Nodal-line and triple point fermion induced anomalous Hall effect in the topological Heusler compound Co$_2$CrGa

Sudipta Chatterjee [ORCID],[*] Jyotirmay Sau, Saheli Samanta, Barnali Ghosh, Nitesh Kumar,[†]
Manoranjan Kumar,[‡] and Kalyan Mandal[§]

Department of Condensed Matter and Materials Physics, S. N. Bose National Centre for Basic Sciences,
JD Block, Sector III, Salt Lake, Kolkata 700106, India

Magnetic topological semimetals have interesting anomalous behavior and can be manipulated by tuning the symmetry-protected nodal crossings. Co$_2$-based full Heusler compounds serve as a fertile playground where various novel topological properties can be investigated. In this paper, we present a systematic investigation of the anomalous Hall effect (AHE) in the ferromagnetic Heusler compound Co$_2$CrGa using combined experimental and theoretical studies. The anomalous Hall resistivity ρ_{yx}^A is observed to scale nearly quadratically with the longitudinal resistivity ρ_{xx}, and further experimental analysis suggests that the AHE in Co$_2$CrGa should be dominated by the intrinsic Karplus-Luttinger Berry phase mechanism. Experimental results also reveal that the anomalous Hall conductivity (AHC) is as large as ∼569 S/cm at 10 K with an intrinsic contribution of ∼526 S/cm and the observed AHC is nearly temperature independent. In addition to the large AHC, we also found an exceptionally large anomalous Hall angle of ∼8.5% and a large anomalous Hall factor of ∼0.23 V^{-1} simultaneously at room temperature. First-principles calculations suggest that the Berry curvature originates from a gapped nodal line and that Weyl nodes which are generated from the triple point near the Fermi level E_F in the presence of spin-orbit coupling are responsible for the observed large AHC in this compound.

I. INTRODUCTION

Three-dimensional topological semimetals (TSMs), new gapless quantum states, have attracted special attention and invited intense research activity in condensed matter physics in recent years because they exhibit fundamentally new physical phenomena with potential applications [1–4]. These TSMs have interesting band dispersion with linear crossing, and depending on the degeneracy of the band crossing points and their distribution in the Brillouin zone (BZ), TSMs are classified into three categories. The first one is zero-dimensional (0D) nodal points which include Weyl points [1,5], Dirac points [6,7], triple points [8], and other higher-degeneracy nodal points [9]. The second one is one-dimensional (1D) nodal-line systems, which include nodal rings [10], nodal chains [11], and nodal nets [11]. The third one is two-dimensional (2D) nodal surfaces [12].

The 0D nodal point systems have been extensively studied during the past decade [6,13,14] due to their nontrivial topological properties and exotic transport phenomena, but investigations of the 1D nodal-line systems have developed mainly in the last few years [15,16]. More recently, the above classification of fermions was expanded to accommodate triply degenerate nodal points. This threefold degeneracy

gives rise to what is known as triple point (TP) fermions [17] and has been confirmed experimentally [18]. However, in Co$_2$-based full Heusler compounds, the existence of TP fermions and their consequences for transport properties have yet to be understood.

Among various magnetic TSMs, Co$_2$-based Heusler compounds have attracted particular interest due to their high Curie temperature and tunable magnetic and electric properties [19,20]. Thus, these materials can be of great use for spin manipulation and spintronics devices. Recently, a few Co$_2$-based full Heusler compounds were also predicted to host Weyl fermions in their band structure [21]. The Berry curvature (BC) associated with this topologically nontrivial state leads to various exotic transport phenomena such as the anomalous Hall effect (AHE), the anomalous Nernst effect, and chiral anomalies [22–30]. The AHE in these compounds originates either from an intrinsic mechanism [31] which can be explained by the Berry phase effect of the occupied electronic Bloch states [32,33] or from extrinsic mechanisms which can be understood to be a result of asymmetric scattering of the conduction electrons in the presence of spin-orbit coupling (SOC) or impurities [34–36]. The AHEs in a few Co$_2$-based full Heusler compounds have been studied both theoretically and experimentally [22–27], but these materials have very different electronic band structures, resulting in large variations in the magnitude of the AHE. For example, Co$_2$MnAl displays a large anomalous Hall conductivity (AHC) of around 1300 S/cm at room temperature due to a gapped nodal ring [26]. Co$_2$MnGa also shows a giant AHC of ∼1600 S/cm at 2 K due to a large BC in momentum space,

———————
[*]schatterjee@bose.res.in
[†]nitesh.kumar@bose.res.in
[‡]manoranjan.kumar@bose.res.in
[§]kalyan@bose.res.in

whereas Co_2VGa exhibits an AHC of around 137 S/cm at 2 K due to a slightly gapped nodal line [23].

In this paper, we report a detailed investigation of the AHE on the full Heusler compound Co_2CrGa using both experimental and theoretical analysis. Experimentally, we found a large AHC $\sim$569 S/cm at 10 K with an intrinsic contribution of 526 S/cm with weak temperature dependence. We also found an exceptionally large anomalous Hall angle (AHA) of $\sim$8.5% and a large anomalous Hall factor (AHF) of $\sim$0.23 V^{-1} simultaneously at room temperature. We also carried out density functional theory calculations based on a first-principles study and observed a topologically protected TP fermion in the absence of SOC in the BZ. We investigated the generation of Weyl nodes from this triple point in the presence of SOC. We also note that the presence of a few symmetry-protected Weyl nodes, and the effect of these Weyl nodes on anomalous transport properties is also discussed.

This paper is organized as follows: first, we discuss the experimental and theoretical methods in Sec. II. The experimental findings and analysis with the simulated result on a gapped nodal line, BC, Wannier charge center (WCC), and anomalous transport are presented in Sec. III. Finally, we conclude with a brief summary in Sec. IV.

II. METHODS

The polycrystalline Co_2CrGa compound was synthesized using a conventional arc-melting furnace in a high-purity argon atmosphere using $\sim$99.99% pure individual elements. To achieve good chemical homogeneity, the sample was remelted six to seven times. The obtained ingot was then sealed in an evacuated quartz tube and annealed at 1173 K for 5 days and then quenched in cold water. The structure and phase purity of Co_2CrGa were characterized by the x-ray diffraction (XRD) technique (Rigaku SmartLab) with a Cu $K\alpha$ source. The details of the structural characterization are discussed in Sec. S1 of the Supplemental Material [37]. Figure S1 shows the XRD pattern of the sample along with its Rietveld refinement, and the obtained lattice parameter is close to that in earlier works [38,39]. The magnetization measurements of the sample were carried out using a vibrating sample magnetometer in a physical property measurement system (PPMS; Quantum Design, San Diego, California). The magnetization data as a function of applied field up to 5 T and temperature down to 10 K were recorded. The sample used for the magnetic measurements has the approximate dimensions $0.4 \times 0.6 \times 4.0$ mm^3. For each $M(H)$ isotherm, we stabilized the temperature for at least 30 min to achieve good thermal equilibrium. The transport measurements were carried out using a 9-T Dynacool PPMS (Quantum Design, San Diego, California) using the electrical transport option. For both the longitudinal and Hall resistivity measurements, the electrical contacts were made with a standard four-probe method using conducting silver epoxy and copper wires. For the measurement of Hall resistivity ρ_{yx}, to effectively eliminate the longitudinal resistivity ρ_{xx} contribution due to the voltage probe misalignment, the final Hall resistivity was obtained from the difference in transverse resistance measured at the positive and negative fields.

We also investigated the electronic band structures and transport properties of Co_2CrGa using the first-principles
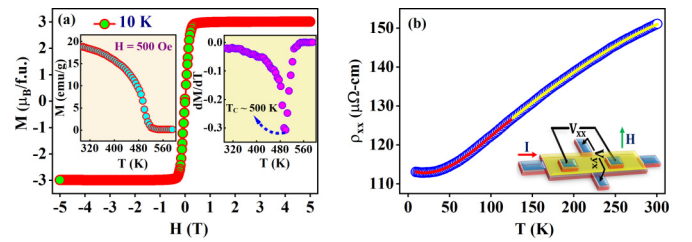

FIG. 1. (a) Magnetic-field-dependent dc magnetization (M vs H) at 10 K. The left inset represents the temperature dependence of dc magnetization (M vs T) measured at 500 Oe, and the right inset shows the derivative magnetization dM/dT vs T. (b) Temperature dependence of the longitudinal resistivity ρ_{xx}. The solid red and yellow lines represent the fittings in two different temperature regions. The inset shows the schematic diagram of the sample device used for longitudinal voltage V_{xx} and Hall voltage V_{yx} measurements.

electronic structure calculations. The projected augmented wave method was implemented to represent the ion-electron interactions. The Vienna Ab initio Simulation Package (VASP) [40] was employed to perform the calculations. The generalized gradient approximation [41] of Perdew-Burke-Ernzerhof [42] type was used for the electronic exchange-correlation functional. A kinetic energy cutoff of 600 eV was utilized for the plane-wave basis. A Γ-centered $12 \times 12 \times 12$ Monkhorst-pack k-point mesh was used for the BZ sampling, and the electronic integral over BZ was estimated by the Gaussian smearing method with a width of 0.05 eV. Cell parameters and internal atomic positions were fully relaxed until the forces on all atoms were smaller than 0.01 eV/A. The calculation was done both with and without SOC. The AHC, energy gap, BC, and WCC were calculated using WANNIER90 [43,44] and WANNIERTOOLS [45] starting from the plane wave basis state. The AHC calculations were carried out with a dense k grid of $501 \times 501 \times 501$ using the limit of the tight-binding model.

III. RESULTS AND DISCUSSION

A. Magnetization and resistivity

Since the topology and magnetism are interconnected, we carried out the magnetization measurements of the sample to evaluate its magnetic nature. The magnetic field dependence of dc magnetization up to a field of 5 T at 10 K is shown in Fig. 1(a). Co_2-based full Heusler compounds generally follow the Slater-Pauling (SP) rule of magnetization [46] as given by $M_t = (Z_t - 24)\mu_B/$f.u., where M_t is the total magnetic moment and Z_t is the total number of valance electrons in the unit cell of the compound. For Co_2CrGa, the value of Z_t is 27. So, according to the SP rule, the total magnetic moment should be $3\mu_B/$f.u. From Fig. 1(a), the value of saturation magnetization M_s at 10 K is estimated to be around $3.01\mu_B/$f.u., which is consistent with the SP rule. The temperature-dependent dc magnetization under an applied field of 500 Oe is also demonstrated in the left inset of Fig. 1(a). It exhibits a continuous paramagnetic to ferromagnetic phase transition at $T_C \sim$ 500 K, estimated from the dM/dT curve, as shown in the right inset of Fig. 1(a). The observed magnetic behavior is quite similar to that in earlier works [38,39]. The temperature variation of the longitudinal resistivity ρ_{xx} from 10 to
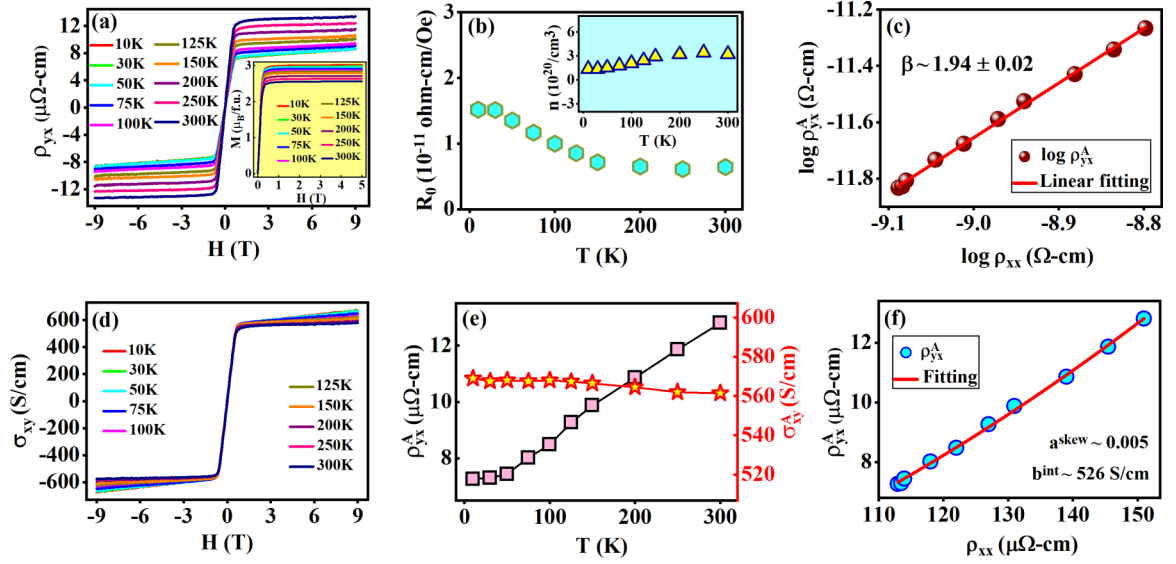
FIG. 2. (a) Magnetic-field-dependent Hall resistivity ρ_{yx} at various temperatures. The inset shows the magnetic field dependence of dc magnetization at different temperatures. (b) Temperature-dependent normal Hall coefficient R_0. The inset shows the calculated temperature-dependent carrier concentration n. (c) Plot of $\log \rho_{yx}^A(T)$ vs $\log \rho_{xx}(T)$; the solid red line is the fit using the relation $\rho_{yx}^A \propto \rho_{xx}^\beta$. (d) Field-dependent Hall conductivity σ_{xy} at various indicated temperatures. (e) Anomalous Hall resistivity ρ_{yx}^A and anomalous Hall conductivity σ_{xy}^A as a function of temperature. (f) Plot of ρ_{yx}^A vs ρ_{xx}. The fitted curve is shown in red.

300 K is presented in Fig. 1(b). The schematic diagram of the sample device used for longitudinal voltage V_{xx} and Hall voltage V_{yx} measurements is shown in the inset of Fig. 1(b). The residual resistivity value at 10 K is ~113 μΩ cm, which yields a residual resistivity ratio [$=\rho_{xx}(300 \text{ K})/\rho_{xx}(10 \text{ K})$] ~ 1.34, which is close to the previously reported value for other Co_2-based full Heusler compounds [25,47]. In general, for a half-metallic ferromagnetic compound the electron-magnon contribution is absent at low temperatures. Therefore, the main contribution to ρ_{xx} appears due to (i) electron-electron (T^2 dependence), (ii) electron-phonon (T dependence), and (iii) double-magnon ($T^{9/2}$ dependence at lower temperatures and $T^{7/2}$ dependence at a higher temperature) scattering [48]. So we have fitted the ρ_{xx} data in two different temperature regions, i.e., between 10 and 125 K and between 125 and 300 K, to understand the different scattering mechanisms of ρ_{xx} in Fig. 1(b). In the temperature range of 10 to 125 K, ρ_{xx} fits very well with the relation, $\rho_{xx}(T) = \rho_0 + AT^{1/2} + BT^2 + CT^{9/2}$ [shown by the solid red line in Fig. 1(b)], while in the high-temperature range, i.e., 125 to 300 K, the best fit is given by $\rho_{xx}(T) = \rho_0 + DT + ET^{7/2}$ [shown by the solid yellow line in Fig. 1(b)]. Here ρ_0 is the residual resistivity, A is the temperature coefficient for the disorder present in the system, B is the temperature coefficient for electron-electron scattering, D is the temperature coefficient for electron-phonon scattering, and C and E are the temperature coefficients for two-magnon scattering. Hence, the temperature-dependent ρ_{xx} data clearly indicate the presence of various scattering mechanisms in the present compound.

B. Anomalous Hall effect

After investigating the structural and magnetic properties of the sample, we carried out a detailed magnetotransport measurement in a wide range of temperatures from 10 to

300 K in order to study the AHE in Co_2CrGa. Figure 2(a) represents the field dependence of Hall resistivity ρ_{yx} up to a field of 9 T at different specified temperatures. At a low field of ~0.7 T, $\rho_{yx}(H)$ increases sharply with an increase in the field, and in the high-field region above ~1 T, $\rho_{yx}(H)$ shows a weak linear field dependence up to 9 T. The field-dependent dc magnetization is shown in the inset of Fig. 2(a) at various temperatures. The similarity in the shapes of the $\rho_{yx}(H)$ and $M(H)$ curves in the low-field region confirms the presence of the AHE in this compound. In addition to the ordinary Hall effect, the Hall resistivity ρ_{yx} in a ferromagnetic material receives a contribution from the spontaneous magnetization M and is expressed as [49]

$$\rho_{yx} = \rho_{yx}^0 + \rho_{yx}^A = R_0 H + R_s \mu_0 M, \qquad (1)$$

where ρ_{yx}^0 and ρ_{yx}^A are the ordinary and anomalous contributions to the total Hall resistivity, with R_0 and R_s being the ordinary and anomalous Hall coefficients, respectively. The values of ρ_{yx}^A and R_0 can be obtained from the linear fit of the ρ_{yx} vs H curve in the high-field region. The y-axis intercept and the slope of the linear fit correspond to ρ_{yx}^A and R_0, respectively. The anomalous Hall coefficient R_s can be obtained by using the relation $\rho_{yx}^A = R_s \mu_0 M_s$ (details are given in Sec. S2 of the Supplemental Material [37]). Figures S2(a) and S2(b) show the temperature variation of ρ_{yx}^A and R_s. The temperature-dependent carrier density n and carrier type can also be determined by using the formulas $R_0 = 1/ne$. Figure 2(b) displays the temperature variation of R_0 from 10 to 300 K. The positive values of R_0 indicate that the holes are the majority charge carriers in the whole temperature range. Using the values of R_0, the carrier density n is evaluated as shown in the inset of Fig. 2(b). It is almost temperature independent, and the estimated carrier density at 10 K is

$\sim 1.37 \times 10^{20}$ cm^{-3}. The corresponding carrier mobility μ_h at 10 K is determined to be $\sim$340 cm^2 V^{-1} S^{-1}.

In order to find the mechanism responsible for the observed AHE in Co$_2$CrGa, we investigate the scaling behavior between ρ_{yx}^A and ρ_{xx} in the whole temperature range on a double-logarithm scale. A linear fitting is applied to determine the exponent β according to the scaling relation $\rho_{yx}^A \propto \rho_{xx}^\beta$ [49], as shown in Fig. 2(c). It is well known that if $\beta = 1$, the origin of the AHE is attributed to the skew scattering, and if $\beta = 2$, the origin of the AHE is due to the intrinsic or side-jump mechanisms [25,27,49]. We found the exponent $\beta = 1.94$, which signifies that the AHE in Co$_2$CrGa is dominated by intrinsic Karplus-Luttinger (KL) or extrinsic side-jump mechanisms. The extrinsic side-jump contribution of the AHC has been shown to be on the order of $e^2/(ha)(\epsilon_{SO}/E_F)$, where ϵ_{SO} is the spin-orbit interaction and E_F is the Fermi energy [50,51]. The terms e, h, and a are the electronic charge, Planck's constant, and the lattice parameter, respectively. For most ferromagnetic metals, the term ϵ_{SO}/E_F is usually on the order of 10^{-2} [25,52]. Thus, the extrinsic side-jump contribution in the AHC should be very small or negligible in comparison to the intrinsic AHC. Hence, the AHE in Co$_2$CrGa is dominated by the intrinsic Berry phase driven KL mechanism.

To understand the microscopic origin of the observed AHE in this compound, we need to look into the variation of the AHC with ρ_{yx}^A and temperature. Therefore, we determine the Hall conductivity σ_{xy} using the tensor conversion relation [23,53]

$$\sigma_{xy} = \frac{\rho_{yx}}{\left(\rho_{xx}^2 + \rho_{yx}^2\right)}. \tag{2}$$

Figure 2(d) depicts the field-dependent Hall conductivity at different temperatures. The field-dependent ρ_{xx} data are given in Sec. S3 of the Supplemental Material [37]. Figure S3 shows ρ_{xx} as a function of magnetic field at different temperatures. ρ_{xx} does not change significantly with magnetic field at a particular temperature. We have extracted the AHC by zero-field extrapolation of high-field Hall conductivity data on the y axis. The value of AHC is found to be $\sim$569 S/cm at 10 K and does not show any significant change up to room temperature (561 S/cm). The temperature dependence of the AHC is given in Sec. S4 of the Supplemental Material [37]. Figure S4 exhibits the temperature-dependent AHC for Co$_2$CrGa. Generally, the AHC changes significantly close to T_C, but far below T_C, it does not change much, which has been observed previously in many Heusler compounds [25,54]. The temperature-dependent AHC and ρ_{yx}^A are plotted in Fig. 2(e), and the variation of AHC is nearly temperature independent, clearly indicating that the origin of AHE in Co$_2$CrGa is intrinsic in nature [55,56]. To distinguish the intrinsic and extrinsic parts of the AHE, we plot ρ_{yx}^A with ρ_{xx} in Fig. 2(f) and fit it with the equation [27,57,58].

$$\rho_{yx}^A = a^{\text{skew}}\rho_{xx} + b^{\text{int}}\rho_{xx}^2, \tag{3}$$

where a^{skew} and b^{int} are the skew-scattering coefficient and intrinsic AHC, respectively. We found $a^{\text{skew}} \sim 0.005$ and intrinsic AHC $b^{\text{int}} \sim 526$ S/cm. Thus, more than $\sim$92% of the total AHC arises due to the intrinsic Berry phase driven mech-

anism. Theoretically, in the resonance condition, the intrinsic AHC is of the order of $e^2/(ha)$, where e is the electronic charge, h is Planck's constant, and a is the lattice constant [51,59]. Taking $a = 5.796$ Å for the studied compound, we estimate the intrinsic AHC to be around 669 S/cm for Co$_2$CrGa, which is close to our experimentally observed value of 526 S/cm.

Finally, we compare the AHE of Co$_2$CrGa with those of other ferromagnetic systems. Here we consider two characteristic parameters, namely, the anomalous Hall angle Θ_{AH} and the anomalous Hall factor S_H. Θ_{AH} can be determined by using the relation $\Theta_{\text{AH}} = \sigma_{xy}^A/\sigma_{xx}$, which measures the relative contribution of the anomalous Hall current with respect to the normal current [49]. Similarly, S_H can also be determined by using the relation $S_H = \frac{R_s \mu_0}{\rho_{xx}^2} = \frac{\sigma_{xy}^A}{M_s}$, which estimates the relative magnitude of the anomalous Hall current with respect to the magnetization [60]. Thus, these two quantities determine the relative strength of the AHE in a compound, which is important for practical applications [61]. Figure 3(a) displays the variation of Θ_{AH} as a function of temperature, and the inset of Fig. 3(a) shows the temperature variation of S_H. The parameter S_H displays a very weak temperature dependence and a similar kind of temperature dependence in S_H was also observed previously in other metallic ferromagnets where the AHE is dominated by the intrinsic Berry phase mechanism [25,54,61,62]. The maximum values of $\Theta_{\text{AH}} \sim$ 8.5% and $S_H \sim 0.23$ V^{-1} are obtained at room temperature, which are some of the largest among metallic ferromagnets. It is very rare to find a metallic ferromagnetic system that has both high Θ_{AH} and S_H simultaneously at room temperature. Even the recently discovered Mn-based antiferromagnets, or half-Heusler antiferromagnets, have either a large Θ_{AH} with a small S_H or vice versa [63,64]. In Fig. 3(b), we also compare the Θ_{AH} and S_H values with values for various previously reported ferromagnetic compounds [25,52,55,60–62,65–69]. Since the intrinsic AHE depends on the band structure of a material to get a better understanding of the origin of the observed large intrinsic AHE, we carried out a first-principles calculation for Co$_2$CrGa.

C. First-principles calculations

Magnetic moments of Co$_2$CrGa are calculated using the first-principles method, and the obtained total magnetic moment is in good agreement with the experimental value; the details of these results are discussed in Sec. S5 of the Supplemental Material [37]. Figure S5 depicts the total density of states of Co$_2$CrGa. To understand the topological aspects of the compound the band dispersions are calculated using a plane wave based pseudopotential [70] in the absence and presence of SOC. Figure 4(b) illustrates several band crossings which form nodal lines in the absence of SOC. There are also different kinds of topological nontrivial crossings in the presence of SOC, shown by blue, green, and magenta circles in Fig. 4(c), and corresponding to these nontrivial crossings, large BC is observed.

In order to further define the class of these nontrivial crossing points the crystal symmetries are considered. The space group of Co$_2$CrGa is $Fm\bar{3}m$ (space group number 225), and
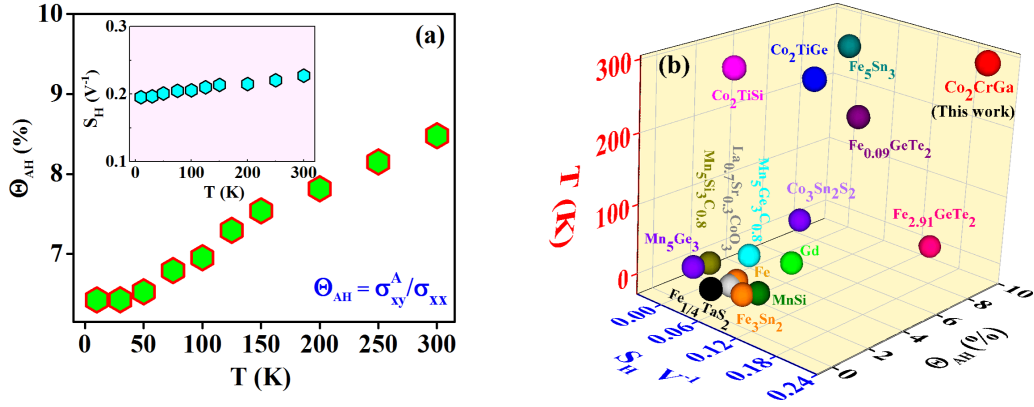
FIG. 3. (a) Temperature-dependent anomalous Hall angle ($\Theta_{AH} = \sigma_{xy}^A/\sigma_{xx}$). The inset shows the temperature dependence of the anomalous Hall factor S_H. (b) Θ_{AH} and S_H for Co_2CrGa are plotted as a function of temperature along with other reported metallic ferromagnets.

the corresponding BZ with a marked high-symmetry point is shown in Fig. 4(a). This symmetry group contains three mirror planes [71], $M_x(k_x = 0)$, $M_y(k_y = 0)$, and $M_z(k_z = 0)$, and three C_4 rotation axes in the absence of finite magnetization. These mirror planes protect the gapless nodal lines in the band structure in the $k_x = 0$, $k_y = 0$, and $k_z = 0$ planes. The presence of SOC along the [001] direction preserves only

the mirror symmetry $M_z = 0$ and C_{4z} rotational symmetry. Therefore, two nodal lines on the $k_x = 0$ and $k_y = 0$ planes are expected to gap out, and the nodal line along the $k_z = 0$ plane should be preserved. The band dispersions in the presence of SOC are shown in Fig. 4(c) around the Fermi energy, and the blue circles along the Γ-W high-symmetry path indicate gapped-out band crossings. Due to small gaps along the nodal
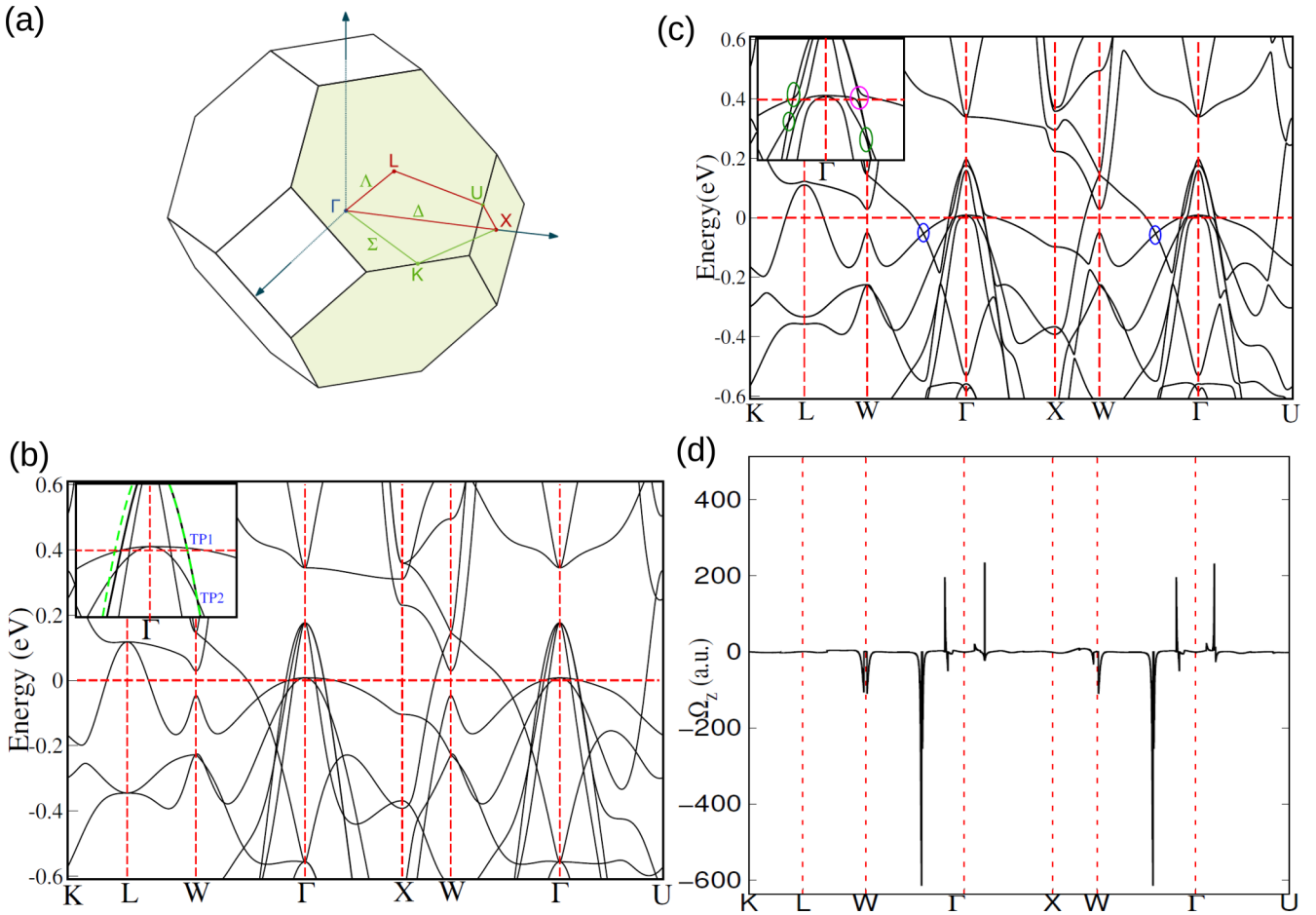

FIG. 4. (a) Brillouin zone of Co_2CrGa. (b) The band structure of Co_2CrGa without SOC. In the inset we also point out the TPs. (c) The band structure of Co_2CrGa with SOC. The Weyl points and the gapped nodal lines are shown by green and blue circles. (d) The Berry curvature along the high-symmetry lines due to the nontrivial crossings.

TABLE I. The Weyl point positions, Chern numbers, and energy relative to E_F of Co_2CrGa.

Weyl point	k_x	k_y	k_z	Chern number	$E - E_F$ (eV)
W_1	1.080	−0.0014	−0.41	−1	−0.10
W_1	−1.080	−0.0077	0.41	1	−0.11
W_2	−0.004	1.0811	0.41	1	−0.06
W_2	0.005	−1.0815	−0.4165	−1	−0.04
W_3	−0.0139	−0.9110	−0.0062	1	−0.01
W_3	−0.0100	0.910	−0.014	−1	−0.02

lines a large Berry curvature in $k_x = 0$ plane is noticed and is discussed in Sec. S6 of the Supplemental Material [37]. Figures S6(a) and S6(b) exhibit the energy gap and the corresponding BC in the $k_x = 0$ plane. In Fig. 4(d), corresponding to gapped nodal lines, a large negative BC is observed along the high-symmetry path Γ-W.

This crystal structure also has a high-symmetry axis of the C_{3v} point group, which has threefold rotational symmetry (C_3) along the [111] direction. Due to this symmetry, twofold-degenerate bands are noted, as shown in the inset of Fig. 4(b) by the thick solid black and dashed green lines. The crossing point of this doubly degenerate band with a nondegenerate band gives rise to a pair of triple points [17] in the absence of SOC, and these are indicated as TP1 and TP2 in the inset of Fig. 4(b). In the presence of SOC along the [001] direction TP1 splits out, as shown in the inset of Fig. 4(c) inside the magenta circle, and TP2 splits into a pair of Weyl points,

which is shown in the inset of Fig. 4(c) in the green circle at −0.08 eV. To understand the texture of these Weyl points, we calculate the normalized BCs which indicate the flux at these two opposite-chirality Weyl points, and their precise position and topological charges are presented in Table I. W_1+ is the source type, where the flux is along the outward direction, as shown in Fig. 5(a), whereas W_1- is the sink type, where the flux is along the inward direction, as shown in Fig. 5(c). Moreover, we also investigate the average position of the WCC obtained with the Wilson-loop method applied on a sphere that encloses these two nodes of opposite chirality. It is observed that the average WCC shifts north to south if the Chern number of W_1 is +1, as shown in Fig. 5(b), while it shifts south to north if the Chern number of W_1 is −1, as shown in Fig. 5(d). We did a similar exercise for the other Weyl nodes denoted by green circles along the high-symmetry path Γ-W, which are discussed in Sec. S7 of the Supplemental
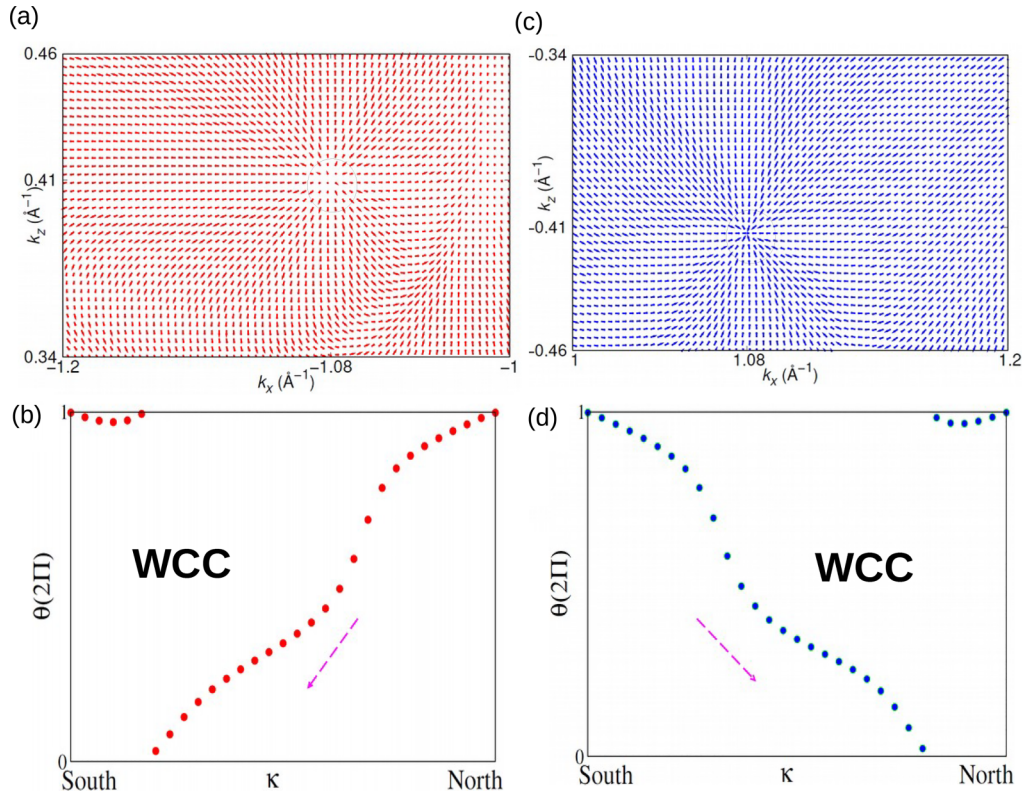

FIG. 5. For Co_2CrGa with SOC normalized Berry curvatures are shown for Weyl point W_1. (a) Source type (W_1+), which is indicated by outward red arrows from the marked black circle. (b) Average position of the Wannier charge center corresponding to the +1 Chern number. (c) Sink type (W_1-), which is indicated by inward blue arrows from the marked black circle. (d) Average position of the Wannier charge center corresponding to a −1 Chern number.
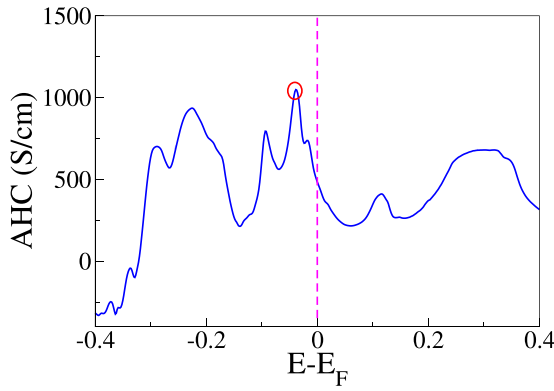
FIG. 6. Energy ($E - E_F$) dependence of the AHC for Co_2CrGa, where the red circle is the position of the gapped nodal line (at an energy of -0.05 eV).

Material [37] (see Fig. S7), and corresponding to these Weyl points, a large BC is noted. The AHC is proportional to the BC, which creates a transverse anomalous velocity in the electronic motion and generates a large AHC. The intrinsic AHC can be evaluated in the linear response theory of Kubo formalism, and AHC in the xy plane can be expressed as

$$\sigma_{xy} = -\frac{e^2}{\hbar} \int \frac{d^3k}{(2\pi)^3} \sum_n \Omega_n^z(k) f_n(k). \quad (4)$$

Ω_n^z is the Berry curvature, and it can be written as

$$\Omega_n^z = -2i \sum_{m \neq n} \frac{\langle \psi_{nk} | v_x | \psi_{mk} \rangle \langle \psi_{mk} | v_y | \psi_{nk} \rangle}{[E_m(k) - E_n(k)]^2}, \quad (5)$$

where $f_n(k)$ is the Fermi-Dirac distribution function, n is the index of the occupied bands, $E_n(k)$ is the eigenvalue of the nth eigenstate $\psi_n(k)$, and $v_i = \frac{1}{\hbar} \frac{\partial H(k)}{\partial k_i}$ is the velocity operator along the i ($i = x, y, z$) direction. To calculate the AHC the SOC is considered along the direction of magnetic polarization [001]. Nearly degenerate bands near the nodal line in the $k_x = 0$, $k_y = 0$ plane have large BC, as shown in Fig. S6 of the Supplemental Material [37], and contribute to the intrinsic AHC. Figure 6 illustrates the energy dependence of the AHC. The giant value (~ 1000 S/cm) of the AHC near the gapped nodal line (~ 0.05 eV below E_F) is shown in Fig. 6 inside the red circle. This value of the AHC is expected to be large due to the maximum BC value at that point, as discussed earlier, but at E_F the AHC value decreases to 504 S/cm due to the positive value of the BC near the Weyl point crossing. The experimentally obtained intrinsic AHC is comparable to that

of the theoretically calculated intrinsic AHC value for this ferromagnetic full Heusler compound.

IV. CONCLUSIONS

In summary, we systematically investigated the AHE in the ferromagnetic full Heusler compound Co_2CrGa both experimentally and theoretically. ρ_{yx}^A scales quadratically with ρ_{xx}, and our detailed experimental analysis suggested that the intrinsic Berry curvature driven KL mechanism is responsible for the observed AHE. Experimentally, a large AHC σ_{xy} ~ 569 S/cm is observed at 10 K with an intrinsic contribution of ~ 526 S/cm. The observed AHC is nearly temperature independent up to room temperature. Moreover, an exceptionally large AHA of $\sim 8.5\%$ and a large AHF of ~ 0.23 V^{-1} were found simultaneously at room temperature, which is very rare in metallic ferromagnets. The first-principles calculations revealed that the AHC in Co_2CrGa is 504 S/cm, which is consistent with the experimentally observed intrinsic AHC value. The theoretical calculations suggested that the BC has a large value in the proximity of the gapped nodal line and makes the highest contribution to the AHC. We also observed the topologically protected TP fermion in its band structure in the absence of SOC and also showed the generation of Weyl points from this TP in the presence of SOC. Moreover, the effect of these nontrivial crossings on anomalous transport properties was discussed. Further, we also noted that the AHC value in this system is highest (~ 1000 S/cm) if E_F shifts to 0.05 eV by hole doping. Thus, further material engineering of this compound would provide a promising pathway to tune its various intriguing topological properties both theoretically and experimentally.

[1] X. Wan, A. M. Turner, A. Vishwanath, and S. Y. Savrasov, Phys. Rev. B **83**, 205101 (2011).

[2] G. Xu, H. Weng, Z. Wang, X. Dai, and Z. Fang, Phys. Rev. Lett. **107**, 186806 (2011).

[3] N. P. Armitage, E. J. Mele, and A. Vishwanath, Rev. Mod. Phys. **90**, 015001 (2018).

[4] B. Q. Lv, T. Qian, and H. Ding, Rev. Mod. Phys. **93**, 025002 (2021).

[5] S.-M. Huang, S.-Y. Xu, I. Belopolski, C.-C. Lee, G. Chang, B. Wang, N. Alidoust, G. Bian, M. Neupane, C. Zhang, S. Jia, A. Bansil, H. Lin, and M. Z. Hasan, Nat. Commun. **6**, 7373 (2015).

[6] Z. Wang, Y. Sun, X.-Q. Chen, C. Franchini, G. Xu, H. Weng, X. Dai, and Z. Fang, Phys. Rev. B **85**, 195320 (2012).

[7] S. M. Young, S. Zaheer, J. C. Y. Teo, C. L. Kane, E. J. Mele, and A. M. Rappe, Phys. Rev. Lett. **108**, 140405 (2012).

[8] H. Weng, C. Fang, Z. Fang, and X. Dai, Phys. Rev. B **93**, 241202(R) (2016).

[9] B. Bradlyn, J. Cano, Z. Wang, M. Vergniory, C. Felser, R. J. Cava, and B. A. Bernevig, Science **353**, aaf5037 (2016).

[10] J. Hu, Z. Tang, J. Liu, X. Liu, Y. Zhu, D. Graf, K. Myhro, S. Tran, C. N. Lau, J. Wei, and Z. Mao, Phys. Rev. Lett. **117**, 016602 (2016).

[11] T. Bzdušek, Q. Wu, A. Rüegg, M. Sigrist, and A. A. Soluyanov, Nature (London) **538**, 75 (2016).

[12] Q.-F. Liang, J. Zhou, R. Yu, Z. Wang, and H. Weng, Phys. Rev. B **93**, 085427 (2016).

[13] Z. Wang, H. Weng, Q. Wu, X. Dai, and Z. Fang, Phys. Rev. B **88**, 125427 (2013).

[14] H. Weng, C. Fang, Z. Fang, B. A. Bernevig, and X. Dai, Phys. Rev. X **5**, 011029 (2015).

[15] C. Fang, Y. Chen, H.-Y. Kee, and L. Fu, Phys. Rev. B **92**, 081201(R) (2015).

[16] Z. Yan, R. Bi, H. Shen, L. Lu, S.-C. Zhang, and Z. Wang, Phys. Rev. B **96**, 041103(R) (2017).

[17] Z. Zhu, G. W. Winkler, Q. S. Wu, J. Li, and A. A. Soluyanov, Phys. Rev. X **6**, 031003 (2016).

[18] B. Lv, Z.-L. Feng, Q.-N. Xu, X. Gao, J.-Z. Ma, L.-Y. Kong, P. Richard, Y.-B. Huang, V. Strocov, C. Fang *et al.*, Nature (London) **546**, 627 (2017).

[19] J. Kübler, G. H. Fecher, and C. Felser, Phys. Rev. B **76**, 024414 (2007).

[20] T. Graf, C. Felser, and S. S. Parkin, Prog. Solid State Chem. **39**, 1 (2011).

[21] Z. Wang, M. G. Vergniory, S. Kushwaha, M. Hirschberger, E. V. Chulkov, A. Ernst, N. P. Ong, R. J. Cava, and B. A. Bernevig, Phys. Rev. Lett. **117**, 236401 (2016).

[22] A. Husmann and L. J. Singh, Phys. Rev. B **73**, 172417 (2006).

[23] K. Manna, L. Muechler, T.-H. Kao, R. Stinshoff, Y. Zhang, J. Gooth, N. Kumar, G. Kreiner, K. Koepernik, R. Car, J. Kübler, G. H. Fecher, C. Shekhar, Y. Sun, and C. Felser, Phys. Rev. X **8**, 041045 (2018).

[24] B. Ernst, R. Sahoo, Y. Sun, J. Nayak, L. Müchler, A. K. Nayak, N. Kumar, J. Gayles, A. Markou, G. H. Fecher, and C. Felser, Phys. Rev. B **100**, 054445 (2019).

[25] S. Roy, R. Singha, A. Ghosh, A. Pariari, and P. Mandal, Phys. Rev. B **102**, 085147 (2020).

[26] P. Li, J. Koo, W. Ning, J. Li, L. Miao, L. Min, Y. Zhu, Y. Wang, N. Alem, C.-X. Liu *et al.*, Nat. Commun. **11**, 1 (2020).

[27] G. K. Shukla, J. Sau, N. Shahi, A. K. Singh, M. Kumar, and S. Singh, Phys. Rev. B **104**, 195108 (2021).

[28] J. Hu, B. Ernst, S. Tu, M. Kuveždić, A. Hamzić, E. Tafra, M. Basletić, Y. Zhang, A. Markou, C. Felser, A. Fert, W. Zhao, J.-P. Ansermet, and H. Yu, Phys. Rev. Appl. **10**, 044037 (2018).

[29] A. Sakai, Y. P. Mizuta, A. A. Nugroho, R. Sihombing, T. Koretsune, M.-T. Suzuki, N. Takemori, R. Ishii, D. Nishio-Hamane, R. Arita *et al.*, Nat. Phys. **14**, 1119 (2018).

[30] K. Manna, Y. Sun, L. Muechler, J. Kübler, and C. Felser, Nat. Rev. Mater. **3**, 244 (2018).

[31] R. Karplus and J. M. Luttinger, Phys. Rev. **95**, 1154 (1954).

[32] T. Jungwirth, Q. Niu, and A. H. MacDonald, Phys. Rev. Lett. **88**, 207208 (2002).

[33] N. Nagaosa, J. Phys. Soc. Jpn. **75**, 042001 (2006).

[34] J. Smit, Physica (Amsterdam) **21**, 877 (1955).

[35] J. Smit, Physica (Amsterdam) **24**, 39 (1958).

[36] L. Berger, Phys. Rev. B **2**, 4559 (1970).

[37] See Supplemental Material at http://link.aps.org/supplemental/10.1103/PhysRevB.107.125138 for XRD, field-dependent longitudinal resistivity, temperature-dependent AHC, spin resolved DOS, and the energy gap and corresponding Berry curvature distribution in presence of SOC.

[38] R. Y. Umetsu, K. Kobayashi, A. Fujita, K. Oikawa, R. Kainuma, K. Ishida, N. Endo, K. Fukamichi, and A. Sakuma, Phys. Rev. B **72**, 214412 (2005).

[39] Y. V. Kudryavtsev, N. V. Uvarov, V. N. Iermolenko, and J. Dubowik, J. Appl. Phys. **108**, 113708 (2010).

[40] J. Hafner, J. Comput. Chem. **29**, 2044 (2008).

[41] J. P. Perdew and Y. Wang, Phys. Rev. B **45**, 13244 (1992).

[42] J. P. Perdew, K. Burke, and M. Ernzerhof, Phys. Rev. Lett. **77**, 3865 (1996).

[43] G. Pizzi, V. Vitale, R. Arita, S. Blügel, F. Freimuth, G. Géranton, M. Gibertini, D. Gresch, C. Johnson, T. Koretsune *et al.*, J. Phys.: Condens. Matter **32**, 165902 (2020).

[44] N. Marzari and D. Vanderbilt, Phys. Rev. B **56**, 12847 (1997).

[45] Q. Wu, S. Zhang, H.-F. Song, M. Troyer, and A. A. Soluyanov, Comput. Phys. Commun. **224**, 405 (2018).

[46] I. Galanakis, P. H. Dederichs, and N. Papanikolaou, Phys. Rev. B **66**, 174429 (2002).

[47] A. Markou, D. Kriegner, J. Gayles, L. Zhang, Y.-C. Chen, B. Ernst, Y.-H. Lai, W. Schnelle, Y.-H. Chu, Y. Sun, and C. Felser, Phys. Rev. B **100**, 054422 (2019).

[48] L. Bainsla, K. Suresh, A. Nigam, M. Manivel Raja, B. C. S. Varaprasad, Y. Takahashi, and K. Hono, J. Appl. Phys. **116**, 203902 (2014).

[49] N. Nagaosa, J. Sinova, S. Onoda, A. H. MacDonald, and N. P. Ong, Rev. Mod. Phys. **82**, 1539 (2010).

[50] P. Nozieres and C. Lewiner, J. Phys. (Paris) **34**, 901 (1973).

[51] S. Onoda, N. Sugimoto, and N. Nagaosa, Phys. Rev. Lett. **97**, 126602 (2006).

[52] Q. Wang, S. Sun, X. Zhang, F. Pang, and H. Lei, Phys. Rev. B **94**, 075135 (2016).

[53] S. N. Guin, K. Manna, J. Noky, S. J. Watzman, C. Fu, N. Kumar, W. Schnelle, C. Shekhar, Y. Sun, J. Gooth *et al.*, NPG Asia Mater. **11**, 16 (2019).

[54] S. Chatterjee, J. Sau, S. Ghosh, S. Samanta, B. Ghosh, M. Kumar, and K. Mandal, J. Phys.: Condens. Matter **35**, 035601 (2023).

[55] Q. Wang, Y. Xu, R. Lou, Z. Liu, M. Li, Y. Huang, D. Shen, H. Weng, S. Wang, and H. Lei, Nat. Commun. **9**, 3681 (2018).

[56] D. Liu, A. Liang, E. Liu, Q. Xu, Y. Li, C. Chen, D. Pei, W. Shi, S. Mo, P. Dudin *et al.*, Science **365**, 1282 (2019).

[57] S. Singh, J. Noky, S. Bhattacharya, P. Vir, Y. Sun, N. Kumar, C. Felser, and C. Shekhar, Adv. Mater. **33**, 2104126 (2021).

[58] G. K. Shukla, A. K. Jena, N. Shahi, K. K. Dubey, I. Rajput, S. Baral, K. Yadav, K. Mukherjee, A. Lakhani, K. Carva, S.-C. Lee, S. Bhattacharjee, and S. Singh, Phys. Rev. B **105**, 035124 (2022).

[59] T. Miyasato, N. Abe, T. Fujii, A. Asamitsu, S. Onoda, Y. Onose, N. Nagaosa, and Y. Tokura, Phys. Rev. Lett. **99**, 086602 (2007).

[60] M. Lee, Y. Onose, Y. Tokura, and N. P. Ong, Phys. Rev. B **75**, 172403 (2007).

[61] K. Kim, J. Seo, E. Lee, K.-T. Ko, B. Kim, B. G. Jang, J. M. Ok, J. Lee, Y. J. Jo, W. Kang *et al.*, Nat. Mater. **17**, 794 (2018).

[62] H. Li, B. Zhang, J. Liang, B. Ding, J. Chen, J. Shen, Z. Li, E. Liu, X. Xi, G. Wu, Y. Yao, H. Yang, and W. Wang, Phys. Rev. B **101**, 140409(R) (2020).

[63] S. Nakatsuji, N. Kiyohara, and T. Higo, Nature (London) **527**, 212 (2015).

[64] T. Suzuki, R. Chisnell, A. Devarakonda, Y.-T. Liu, W. Feng, D. Xiao, J. W. Lynn, and J. Checkelsky, Nat. Phys. **12**, 1119 (2016).

[65] S. A. Baily and M. B. Salamon, Phys. Rev. B **71**, 104407 (2005).

[66] Y. Onose and Y. Tokura, Phys. Rev. B **73**, 174421 (2006).

[67] J. G. Checkelsky, M. Lee, E. Morosan, R. J. Cava, and N. P. Ong, Phys. Rev. B **77**, 014433 (2008).

[68] S. Sangiao, L. Morellon, G. Simon, J. M. De Teresa, J. A. Pardo, J. Arbiol, and M. R. Ibarra, Phys. Rev. B **79**, 014431 (2009).

[69] C. Sürgers, G. Fischer, P. Winkel, and H. v. Löhneysen, Phys. Rev. B **90**, 104421 (2014).

[70] P. E. Blöchl, Phys. Rev. B **50**, 17953 (1994).

[71] G. Chang, S.-Y. Xu, H. Zheng, B. Singh, C.-H. Hsu, G. Bian, N. Alidoust, I. Belopolski, D. S. Sanchez, S. Zhang, H. Lin, and M. Z. Hasan, Sci. Rep. **6**, 38839 (2016).